

CONVECTION EFFECTS IN THREE-DIMENSIONAL DENDRITIC GROWTH

Yili Lu¹, C. Beckermann^{1*}, and A. Karma²

¹Department of Mechanical and Industrial Engineering, University of Iowa, Iowa City, IA 52242-1527, U.S.A. ²Department of Physics and Center for Interdisciplinary Research on Complex Systems, Northeastern University, Boston, MA 02115, U.S.A.

Abstract

A phase-field model is developed to simulate free dendritic growth coupled with fluid flow for a pure material in three dimensions. The preliminary results presented here illustrate the strong influence of convection on the three-dimensional (3D) dendrite growth morphology. The detailed knowledge of the flow and temperature fields in the melt around the dendrite from the simulations allows for a detailed understanding of the convection effects on dendritic growth.

Introduction

Dendrites are the most common microstructure found in engineering materials. The shape, size and orientation of the dendrites determine to a large extent the physical and chemical properties of cast and welded metals. While numerous experimental, numerical and analytical studies have been performed to understand dendritic growth in diffusion-controlled situations¹⁻¹², the pattern selection and microstructure evolution are not well understood for convection-controlled growth. Convection in the melt during solidification can be caused by buoyancy forces, dendrite movement, shrinkage, or a variety of imposed flows.

In the past ten years, the phase-field method¹³⁻¹⁶ has become a popular computational tool to simulate microstructure formation in solidification. The main advantage of the phase-field method is that it avoids direct tracking of the sharp solid-liquid interfaces¹⁷⁻¹⁹. Based on an analysis of the thin interface limit, Karma and Rappel²⁰⁻²² proposed a computationally efficient phase-field method that allows for quantitative modeling of dendritic crystal growth. Beckermann et al.²³ employed the phase-field method to study convective effects on dendritic growth in two dimensions (2D). The numerical results show that convection can significantly alter the operating state of a dendrite and dendritic sidebranching. Very recently, Jeong et al.²⁴ investigated the effect of fluid flow on 3D dendritic growth using an adaptive-grid finite element method. They found that the flow and dendrite growth shapes in three dimensions are very different from those in two dimensions.

In this paper, our previous simulations of 2D dendritic growth with convection²³ are extended to three dimensions. Preliminary results are presented that illustrate the effects of convection on dendritic growth.

Governing equations

The governing equations for flow and heat transfer are the same as those derived in Ref.²³, while the phase-field equation is taken from the work of Karma and Rappel²⁰⁻²². The effects of flow in the phase-field equation are neglected. All equations are valid in the single-phase solid and liquid regions as well as in the

Keywords: dendritic growth, phase-field method, convection, flight

* Corresponding author. e-mail: becker@engineering.uiowa.edu

diffuse interface region, where the phase-field variable, ψ , varies from -1 to $+1$. An auxiliary variable, the solid fraction ε_s , is introduced as $\varepsilon_s = (1 + \psi)/2$. The equations can be summarized as follows.

Mass conservation:

$$\nabla \cdot [(1 - \varepsilon_s) \cdot \vec{v}_l] = 0, \quad (1)$$

where \vec{v}_l is the intrinsic velocity of the liquid.

Momentum conservation:

$$\begin{aligned} \frac{\partial}{\partial t} [(1 - \varepsilon_s) \vec{v}_l] + \nabla \cdot [(1 - \varepsilon_s) \vec{v}_l \vec{v}_l] = & -(1 - \varepsilon_s) \nabla p \\ & + v_l \nabla^2 [(1 - \varepsilon_s) \vec{v}_l] - v_l \frac{h \varepsilon_s^2 (1 - \varepsilon_s)}{W_0^2} \vec{v}_l, \end{aligned} \quad (2)$$

where v_l , p , and t are the kinematic viscosity, pressure, and time, respectively. The parameter W_0 is representative of the interface thickness (see below). The last term on the right-hand side of equation (2) is a distributed interfacial force term that forces the liquid velocity to vanish across the diffuse interface as the solid approached. The coefficient h is a constant equal to 5.514, which was determined from an asymptotic analysis that forces the velocity profile to approach that for a no-slip condition at a sharp interface located at $\varepsilon_s = 0.5$.

Energy conservation:

$$\frac{\partial u}{\partial t} + \nabla \cdot [(1 - \varepsilon_s) v_l u] = D \nabla^2 u + \frac{\partial \varepsilon_s}{\partial t} \quad (3)$$

where D is the thermal diffusivity. The dimensionless temperature u is defined as $u = (T - T_M)/(L/c_p)$, where T_M , L , and c_p are the melting temperature, latent heat, and specific heat at constant pressure, respectively.

Phase-field equation:

$$\tau(\mathbf{n}) \frac{\partial \psi}{\partial t} = [\psi - \lambda u (1 - \psi^2)] (1 - \psi^2) + \nabla \cdot [W^2(\mathbf{n}) \nabla \psi] + \sum_{\xi=x,y,z} \frac{\partial}{\partial \xi} \left[|\nabla \psi|^2 W(\mathbf{n}) \frac{\partial W(\mathbf{n})}{\partial (\partial_\xi \psi)} \right], \quad (4)$$

where λ is a dimensionless parameter that controls the strength of the coupling between the phase and temperature fields, and \mathbf{n} is the interface normal. The interface thickness parameter W depends on the orientation of the interface and is given by $W(\mathbf{n}) = W_0 a_s(\mathbf{n})$. In the limit of vanishing interface kinetics, $\tau(\mathbf{n})$ is chosen as $\tau(\mathbf{n}) = \tau_0 a_s^2(\mathbf{n})$, with

$$a_s(\mathbf{n}) = (1 - 3\varepsilon_4) \left[1 + \frac{4\varepsilon_4}{1 - 3\varepsilon_4} \frac{(\partial_x \psi)^4 + (\partial_y \psi)^4 + (\partial_z \psi)^4}{(\nabla \psi)^4} \right], \quad (5)$$

where ε_4 is the anisotropy strength. All other details can be found in the original references.^{18,19}

Numerical method

The energy and phase-field equations are solved using an explicit finite difference method on uniform grids that are different from each other. The node spacing for the energy equation is exactly twice as large as the one for the phase-field equation, as illustrated in Figure 1. This can be done without loss of accuracy, because the thermal diffusion length is much larger than the diffuse interface thickness. The temperatures on the fine-mesh nodes for use in the phase-field equation are obtained by linear interpolation. Extensive numerical tests were performed to validate this approach for the ranges of the governing parameters considered here.

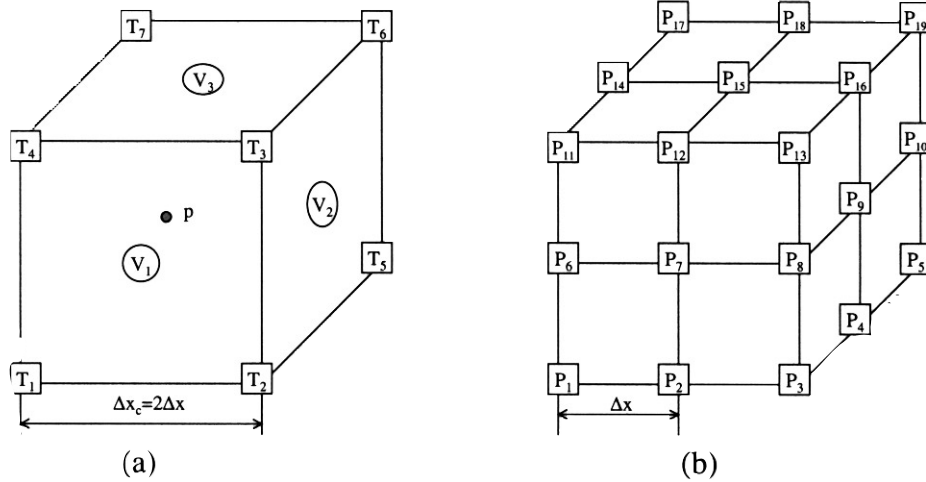


Figure 1. Configurations in the fine and coarse meshes. (a). One coarse grid (big cube) in finite difference scheme (or one element in finite element scheme). Nodes for temperature are defined on 8 corners, namely $T_1 \sim T_8$ (T_8 is not shown in the Figure). Nodes for velocity are defined on the 6 surface centers of the coarse grid, namely $V_1 \sim V_6$ ($V_4 \sim V_6$ are not shown in the Figure). Pressure p is defined on the volume center of the coarse grid. (b). 8 fine grids (cubes) that correspond to one coarse grid. Nodes for the phase-field variable are defined on every corner of the fine grid, namely $P_1 \sim P_{27}$ ($P_{20} \sim P_{27}$ are not shown for clarity).

The mass and momentum equations are solved using a modified version of the finite element CFD code FEAST²⁵. This code was originally developed by Turek and coworkers in the Department of Mathematics at the University of Dortmund, Germany. Descriptions of the discretization technique, the error control method, and the multi-grid solution scheme can be found online²⁵. The code was modified to accommodate the non-standard forms of the mass and momentum equations, Eqs. (1) and (2). As shown in Figure 1a, the velocity is defined at the center of the six surfaces of the element, while the pressure is defined at the center of the volume element. Most importantly, the element edge length is again twice as large as the node spacing used in the solution of the phase-field equation. Since most of the total computational effort is associated with the solution of the flow equations, this method offers tremendous savings in both computer time and memory. It was verified through extensive numerical tests that the use of a coarser mesh for the flow equations does not sacrifice accuracy for the cases considered here. The velocities were interpolated to the appropriate locations for use in the solution of the energy equation. The flow equations are solved in a fully implicit manner. As found previously by the present authors²³, this allows for the use of a larger time step (about five times as large) for the flow equations than for the phase-field and energy equations; however, this procedure was not utilized in the present study.

Numerous benchmark problems were solved using the present 3D code in order to validate the numerical method. Only one of these, flow around a cylinder at low Reynolds numbers, is described here. The cylinder was represented by a (stationary) distribution of the phase field variable, which varies in a hyperbolic tangent fashion across the cylinder-fluid interface. In other words, the cylinder was not explicitly discretized. For the present simulations at low Reynolds numbers, the computational domain has to be much larger than the cylinder so that the flow field is not influenced by the boundaries²⁶; hence, a non-uniform grid of hexahedral elements was utilized. A two-dimensional cut of the mesh is plotted in Figure 2a. Since the elements are densely concentrated at the center of the cut where the cylinder is present,

an enlarged view of this region of the mesh is shown in Figure 2b. The flow is from left ($x=0$ plane) to right ($x=10$ plane) in this Figure. A uniform inlet velocity and a zero-velocity gradient at the outlet are used as boundary conditions on these two planes. Slip boundary conditions are applied at the bottom ($y=0$ plane) and top ($y=10$ plane) boundaries. Two-dimensional results for an infinitely long cylinder are desired for the comparison with the benchmark results. Hence, slip boundary conditions are applied on the front and back boundaries. Then, the size of the domain in the z -direction (parallel to the axis of the cylinder) is arbitrary.

Using the computed flow results, the drag coefficient, C_D , of the cylinder was determined as a function of the Reynolds number. A comparison of the present results for the drag coefficient with previous experimental measurements²⁷⁻²⁸ is shown in Figure 3. The agreement is good for all Reynolds numbers.

Results

Figure 4 shows the physical domain and conditions used in the present simulation of free dendritic growth in the presence of melt convection. A spherical seed at the melting temperature ($u=0$) is located in the center of a cubic domain of volume 204.8^3 . The $[100]$, $[010]$ and $[001]$ crystalline directions are aligned with the x , y , z coordinates, respectively. Undercooled melt enters the domain at the $x=0$ plane with a uniform velocity of $U=1$ and dimensionless temperature of $u_{in}=\Delta=-0.55$. The melt exits at the opposing end of the domain. Symmetry or slip boundary conditions are imposed on the four planes normal to the inlet and outlet. For the present low Reynolds number flow, symmetry allows the computations to be performed in only a quarter of the domain. Other conditions include $D=4$, $\varepsilon_4 = 0.05$, and $Pr = \nu/D = 2.5$. The calculations were performed on a uniform grid of $128 \times 64 \times 64$ nodes for the flow and temperature fields and of $256 \times 128 \times 128$ nodes for the phase field.

Figure 5 shows computed dendrite shapes at various times. Since the dendrite would be completely symmetric in the absence of flow, it is obvious that the convection dramatically alters the growth morphology. The arms growing into the flow, in the upstream direction, grow much faster than the cross-stream arms. The arm pointing in the downstream direction grows so slowly that it is virtually non-existent.

The flow field is illustrated in Figures 6 to 8. Figure 6 shows the general characteristic of the streamlines around the dendrite. Figures 7 and 8 show representative streamlines on the upstream and downstream sides of the dendrite, respectively. The flow advects heat from the upstream to the downstream side. Consequently, the temperature field around the dendrite is very asymmetrical, as shown in Figure 9. The temperature gradients are largest at the upstream tip, resulting in the large growth velocities there. The temperature in the wake of the dendrite is more uniform and closer to the melting point. Compared to the downstream arm, the cross-stream arms suffer much less from the convective transport of heat. This can be seen from the streamlines in Figures 6 to 8. Most of the fluid that passes near the upstream dendrite arm and gets heated, flows through the space between the four cross-stream arms. The melt that passes directly by the cross-stream arm tips originates primarily from the far field and is not heated by any upstream structure. As can be seen from Figure 6, the shape of the cross-stream arm is very asymmetrical in the z plane, which again is caused by advection of heat around those arms.

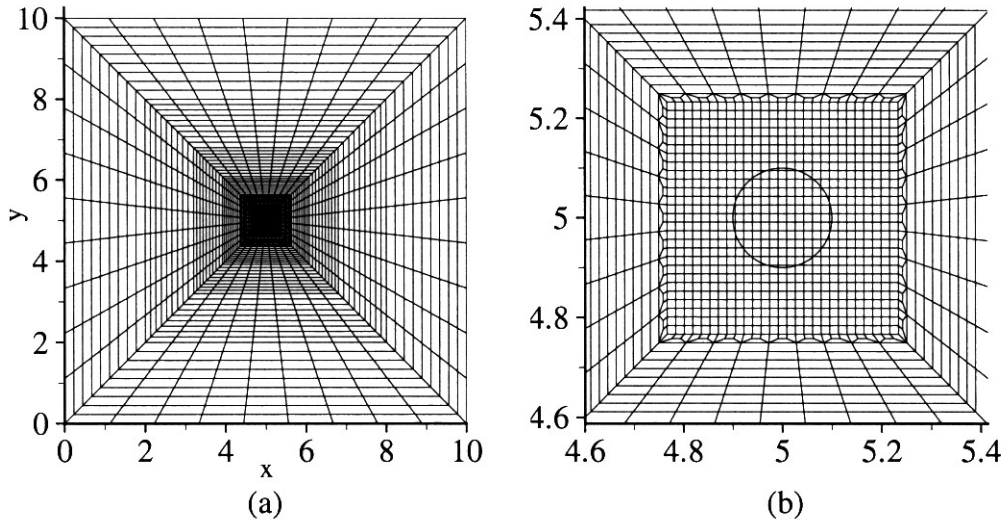


Figure 2. 2D view of the non-uniform mesh for calculating the cylinder drag at low Reynolds numbers. 3D mesh is simply extended by this 2D mesh in the z direction. The domain size is $10 \times 10 \times 0.8$. (a). Complete 2D view of the mesh. (b). Better view of the 2D mesh in the center region of the domain. The circle (cylinder in 3D) is defined by a (stationary) distribution of the phase-field variable, which varies in a hyperbolic tangent fashion.

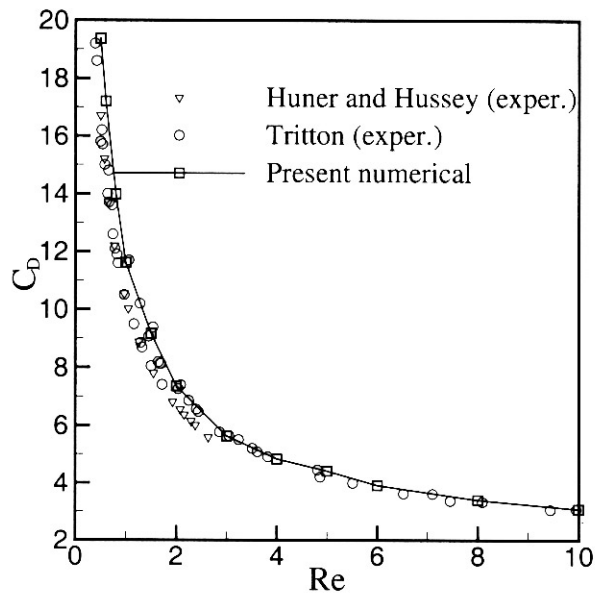


Figure 3. Cylinder drag coefficient at low Reynolds numbers.

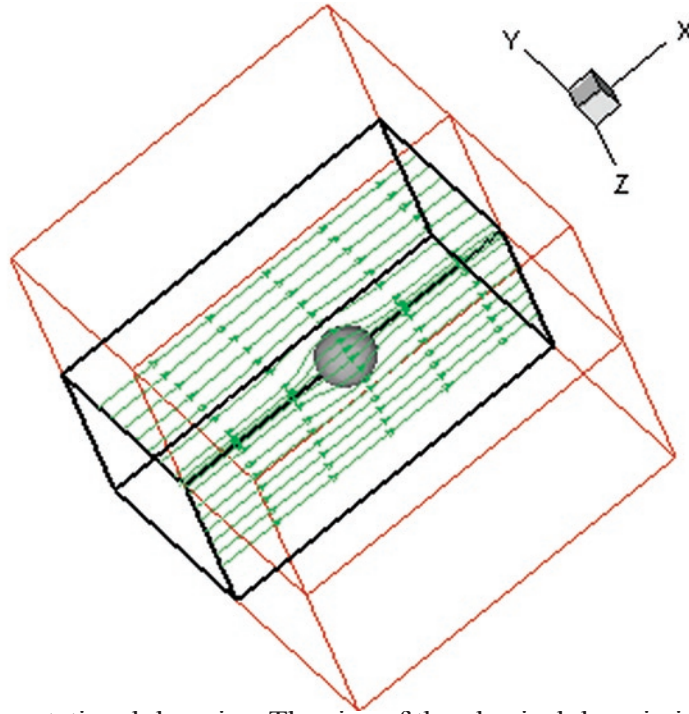


Figure 4. Physical and computational domains. The size of the physical domain is 204.8^3 . The computation domain is only one quarter of the physical domain (the first octant with black color) due to symmetry. Fluid with uniform velocity ($U=1$) passes over the sphere seed initially fixed in the center of the physical domain.

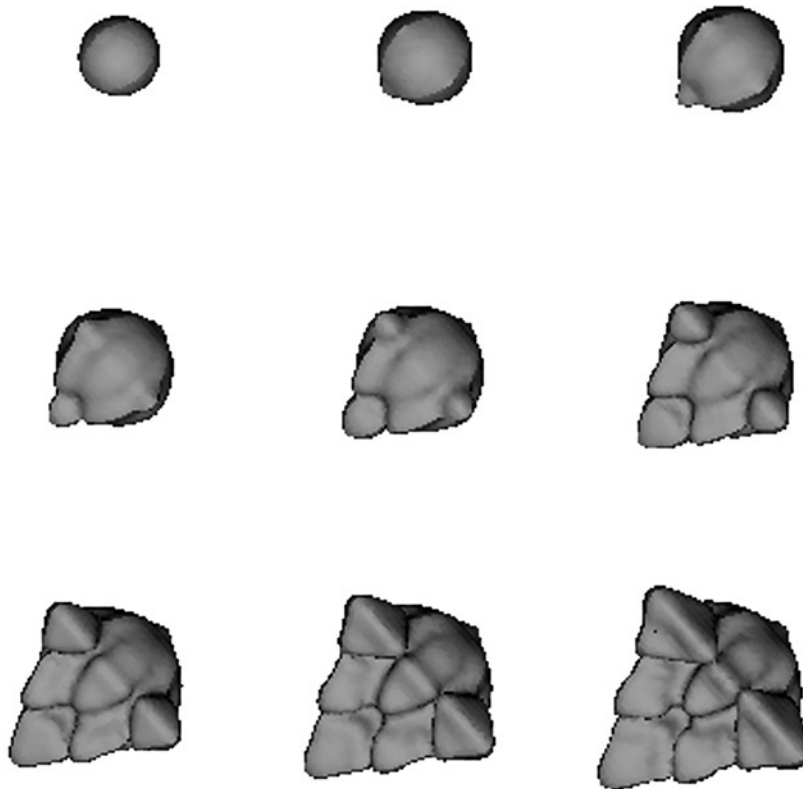


Figure 5. Microstructure evolution of the dendrite under convection. The dimensionless time interval is $\Delta t/\tau_0 = 8$. The input parameters are $\Delta = -0.55$, $D=4$, $\varepsilon_4 = 0.05$, $Pr = \nu/D = 2.5$, $U=1$, and $\lambda = 6.383$.

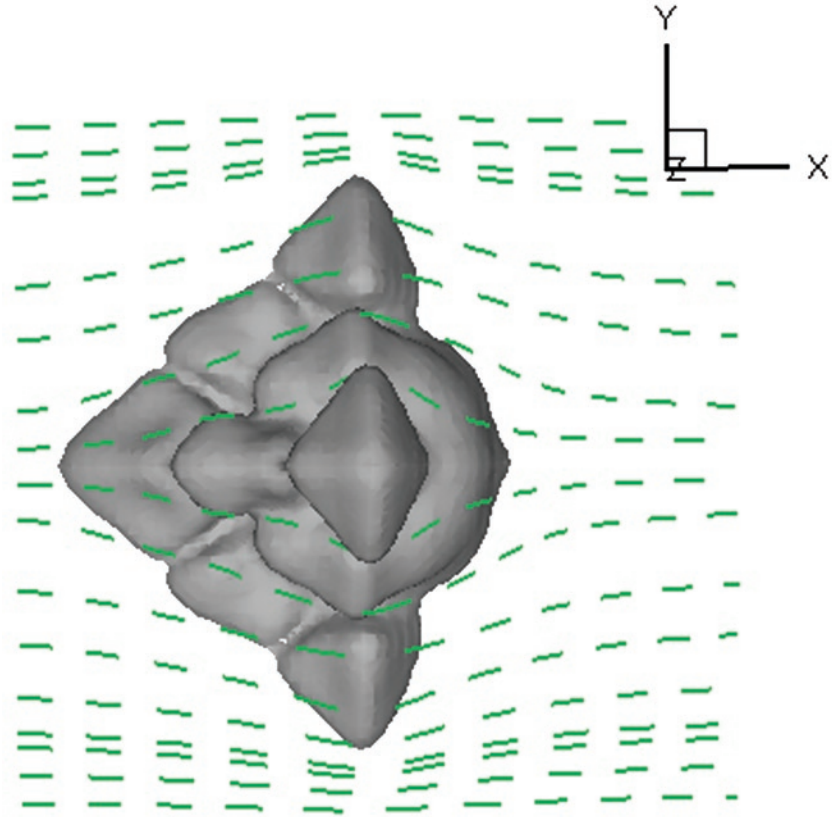


Figure 6. Streamlines around the dendrite viewed in z direction.

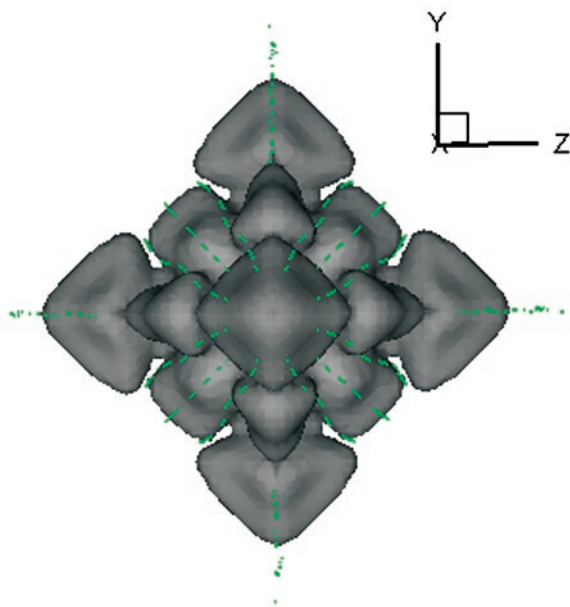


Figure 7. Streamlines near the upstream arm viewed from negative x direction

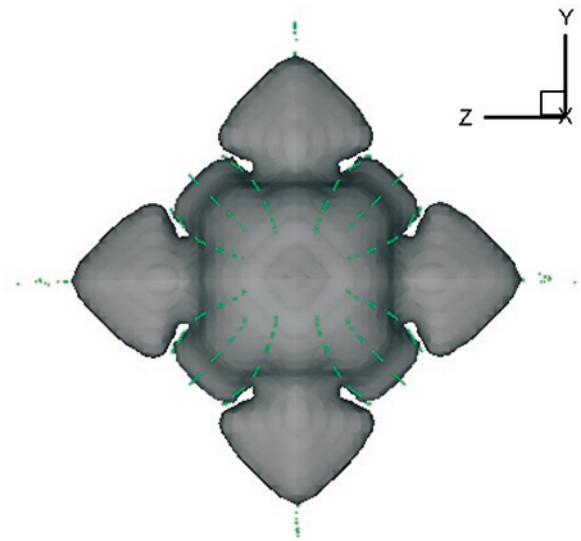


Figure 8. Streamlines near the downstream arm viewed from positive x direction

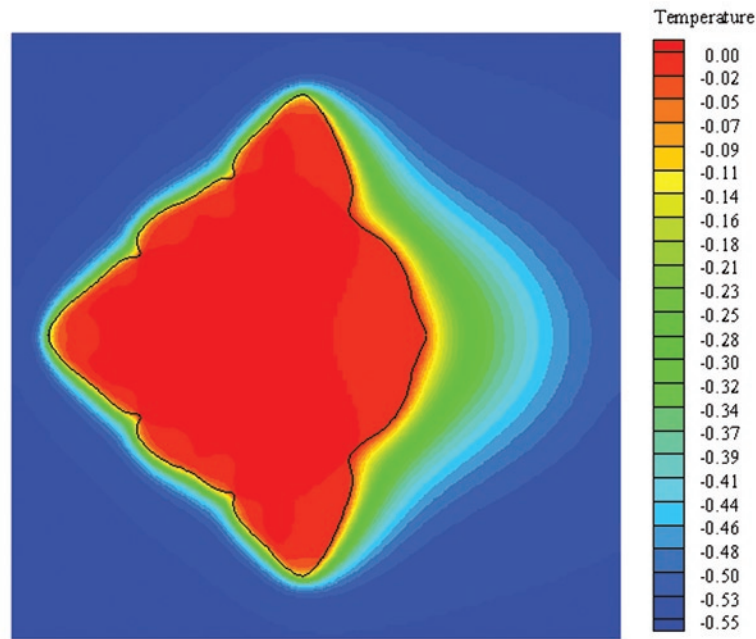
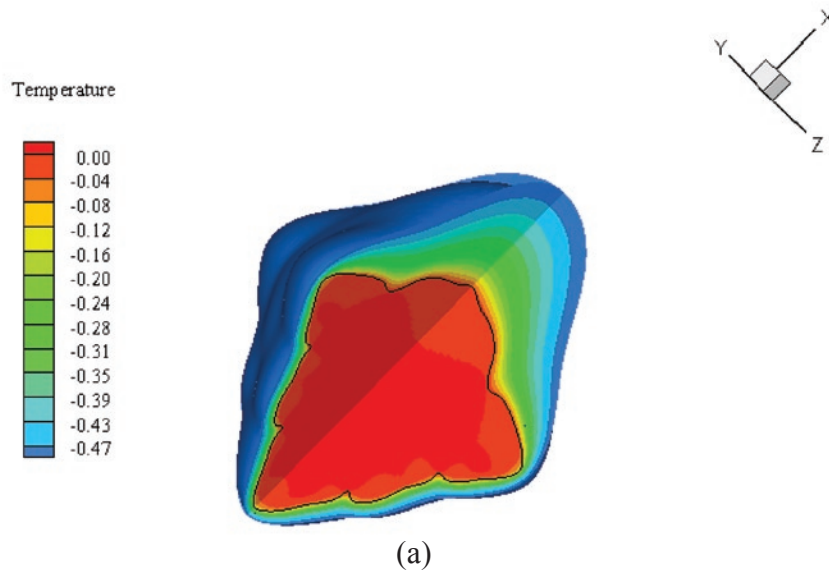


Figure 9. Temperature field around the dendrite. The black line represents the interface contour. (a). 3D temperature field around the dendrite. The first octant was cut for better visualization. Temperature below -0.47 was not shown for clarity. (b). 2D temperature field at $y=0$ plane.

Conclusions

A phase-field method has been developed to simulate free dendritic growth in three dimensions in the presence of a forced melt flow. Convection is found to significantly alter the growth morphology of dendrites. While the flow and temperature results presented here allow for a qualitative understanding of the effects of convection, a comparison of the predictions with relevant dendrite growth theories and experimental results is still underway.

Acknowledgements

This research was supported by NASA under Contract No. NCC8-94. The authors wish to thank Prof. Turek for his help with the FEAST code.

References

1. Tiller, W. A., Jackson, K. A., Rutter, J. W., Chalmers, B., "The redistribution of solute atoms during the solidification of metals", *Acta Metall.* 1, 428-437(1953).
2. Mullins, W. W., Sekerka, R. F., "Morphological stability of a particle growing by diffusion or heat flow", *J. Appl. Phys.* 34, 323-329(1963).
3. Mullins, W. W., Sekerka, R. F., "Stability of a planar interface during solidification of a dilute binary alloy", *J. Appl. Phys.* 35, 444-451(1964).
4. Glicksman, M. E., Schaefer, R. J., Ayers, J. D., "Dendritic growth- A test of theory", *Metall. Trans.* A7, 1747-1759(1976).
5. Glicksman, M. E., and Singh, N. B., "Effects of crystal-melt interfacial energy anisotropy on dendritic morphology and growth kinetics" *J. Crystal Growth* 98, 277-284(1989).
6. Trivedi, R., "Growth of dendritic needles from a supercooled melt", *Acta. Metall.* 18, 287-296(1970).
7. Trivedi, R., "Theory of dendritic growth during the directional solidification of binary alloys", *J. Crystal Growth* 49, 219-232(1980).
8. McFadden, G. B., Wheeler, A. A., Braun, R. J., Coriell, S. R., and Sekerka, R. F., "Phase-field models for anisotropic interfaces", *Phys. Rev. E* 48, 2016-2024(1993).
9. Oldfield, W., "Computer model studies of dendritic growth", *Mater. Sci. Eng.* 11, 211-218(1973).
10. Langer, J. S., Müller-Krumbhaar, H., "Theory of dendritic growth-i. elements of stability analysis", *Acta Metall.* 26, 1681-1687(1978).
11. Ivantsov, G. P., "Temperature field around spherical, cylindrical and needle-shaped crystals which grow in supercooled melt", *Dokl. Akad. Nauk SSSR* 58, 567-569(1947).
12. Kessler, D. A., Koplik, J. and Levine, H., "Pattern selection in fingered growth phenomena", *Adv. in Phys.* 37(2), 255-339(1988).
13. Fix, G. J., in *Free Boundary Problems: Theory and Application*, Vol. II, edited by A. Fasano and M. Primicerio, Piman, Boston, 580-589(1983).
14. Collins, J. B. and Levine, H., "Diffuse interface model of diffusion-limited crystal growth", *Phys. Rev. B* 31, 6119-6122(1985).
15. Kobayashi, R., "Modeling and numerical simulations of dendritic crystal growth", *Physica D* 63, 410-423(1993).
16. Murray, B. T., Wheeler, A. A., Glicksman, M. E., "Simulation of experimentally observed dendritic growth behavior using a phase-field model", *J. Crystal Growth* 47, 386-400(1995).
17. Sethian, J. A. and Strain, J., "Crystal growth and dendritic solidification", *J. Comp. Phys.* 98, 231-253(1992).
18. Almgren, R., "Variational algorithms and pattern formation in dendritic solidification", *J. Comp. Phys.* 106, 337-354(1993).
19. Roosen, A. R. and Taylor, J. E., "Modeling crystal growth in a diffusion field using fully faceted interface", *J. Comp. Phys.* 114, 113-128(1994).
20. Karma, A. and Rappel, W. J., "Phase-field method for computationally efficient modeling of solidification with arbitrary interface kinetics", *Phys. Rev. E* 53, 3017-3020(1996).
21. Karma, A. and Rappel, W. J., "Phase-field model of dendritic sidebranching with thermal noise", *Phys. Rev. E* 60(4), 3614-3625(1999).

22. Karma, A. and Rappel, W. J., “Quantitative phase-field modeling of dendritic growth in two and three dimensions”, *Phys. Rev. E* 57(4), 4323-4349(1998).
23. Beckermann, C., Diepers, H. J., Steinbach, J., Karma, A. and Tong, X., “Modeling melt convection in phase-field simulations of solidification”, *J. Comp. Phys.* 154, 468-496(1999).
24. Jeong, J. H., Goldenfeld, N., Dantzig, J. A., “Phase field model for three-dimensional dendritic growth with fluid flow”, *Phys. Rev. E* 64:041602(2001).
25. <http://www.featflow.de>
26. Lange, C. F., Durst, F., and Breuer, M., “Momentum and heat transfer from cylinders in laminar crossflow at $10^{-4} \leq Re \leq 200$ ”, *Int. J. of Heat and Mass Transfer* 41, 3409-3430(1998).
27. Tritton, D. J., “Experiments on the flow past a circular cylinder at low Reynolds number” *J. Fluid Mechanics* 6, 547-567(1959).
28. Huner, B., and Hussey, R. G., “Cylinder drag at low Reynolds number”, *The Physics of Fluids*, 20(8), 1211-1218(1977).